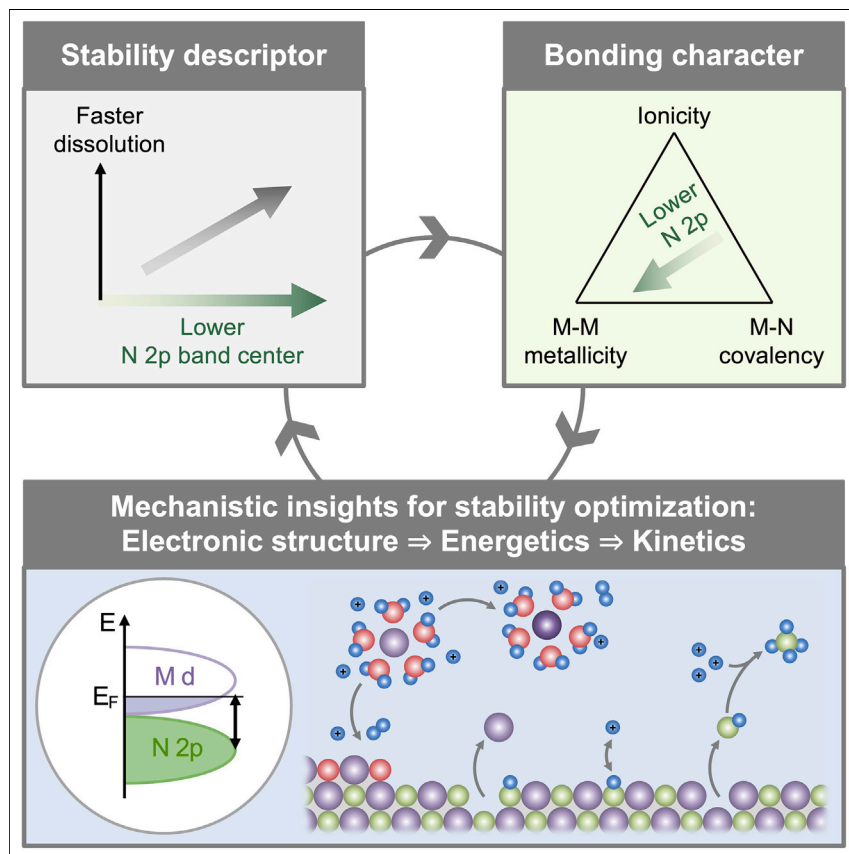


Article

Design principles for transition metal nitride stability and ammonia generation in acid



Transition metal nitrides have suffered from severe nitride dissolution and subsequent ammonia generation in acidic electrolytes, limiting the use of earth-abundant nitride catalysts in proton exchange membrane fuel cells and electrolyzers. Combining theory and experiment, we have established design principles governing the extent and kinetics of nitride decomposition and ammonia production in acid. Guided by these insights, new nitride catalysts can be rationally designed with optimized stability in acid to electrify and decarbonize the production and utilization of chemicals and fuels.

Jiayu Peng, Juan J. Giner-Sanz,
Livia Giordano, ..., Yang Yu,
Yuriy Román-Leshkov, Yang
Shao-Horn

yroman@mit.edu (Y.R.-L.)
shaohorn@mit.edu (Y.S.-H.)

Highlights

Nitrogen 2p band center governs nitride dissolution by tuning the bonding character

Lowering the solubility of metal ions passivates nitrides and hinders dissolution

A new mechanistic picture of nitride dissolution and ammonia formation is proposed

Article

Design principles for transition metal nitride stability and ammonia generation in acid

Jiayu Peng,¹ Juan J. Giner-Sanz,^{2,3} Livia Giordano,^{2,4} William P. Mounfield III,⁵ Graham M. Leverick,⁶ Yang Yu,¹ Yuryi Román-Leshkov,^{5,*} and Yang Shao-Horn^{1,2,6,7,*}

SUMMARY

Transition metal nitrides have shown promise as electrocatalysts in proton exchange membrane fuel cells and electrolyzers, but the instability of these nitrides in acid has limited their function for such technologies. On the other hand, having fast, complete nitride dissolution and ammonia formation in acid can offer new opportunities for distributed, on-demand ammonia generation. Optimizing nitride chemistries for these clean energy applications requires design principles for nitride dissolution and ammonia formation in acid. Here, we report that lowering the nitrogen 2p band center of transition metal nitrides relative to the Fermi level weakens metal–nitrogen bonds and increases labile metallic character, reducing dissolution reaction barriers and boosting ammonia formation kinetics in acid. Increasing the solubility of dissolved metal cations further facilitates the decomposition of nitrides in acid by prohibiting surface oxide passivation. These findings highlight essential future directions for preventing nitride dissolution or facilitating ammonia production for diverse acidic applications.

INTRODUCTION

Transition metal nitrides have emerged as promising earth-abundant catalysts to reduce or eliminate the use of precious metals (e.g., Pt) in proton exchange membrane fuel cells and electrolyzers due to their low cost, high electrical conductivity, sinter resistance, and noble-metal-like electronic structures.^{1,2} Unfortunately, the use of transition metal nitrides in such technologies has been hampered by the instability of these nitrides in acid.^{3–8} For example, the durability of Pt/TiWN core-shell nanoparticles for the oxygen reduction reaction has suffered from the dissolution of nitride cores in acid.⁷ Similarly, the long-term oxygen reduction activity of Ni₃N in acid has been shown to be significantly more unstable than that in base.⁸ These observations are corroborated by the decomposition of nitride catalysts for electrochemical nitrogen reduction in acid, which has resulted in false positives in discovering new electrocatalysts.⁹ For instance, while nitrides such as VN,¹⁰ NbN,¹¹ and Mo₂N¹² have been computationally predicted to catalyze the reduction of nitrogen to ammonia, the experimentally observed ammonia has been attributed to the dissolution of nitrides in acid.^{3–5} Therefore, it is imperative to establish stability descriptors of transition metal nitrides in acid, which not only offer a fundamental understanding of nitride dissolution but also provide new guiding principles to optimize their intrinsic stability and relevant ammonia generation in acid for diverse applications.

Here, we investigated nine transition metal nitrides with diverse structures and chemistries, including TiN, VN, CrN, ZrN, NbN, WN, Ta₃N₅, Fe₂N, and Ni₃N

CONTEXT & SCALE

Proton exchange membrane fuel cells and electrolyzers hold promise for decarbonizing the production and utilization of chemicals and fuels, including hydrogen and ammonia, but these technologies still require the deployment of earth-abundant, non-precious catalysts to lower their cost. To tackle this challenge, transition metal nitrides have been widely explored as electrocatalysts for such technologies. However, the dissolution of nitrides in acid has led to electrode degradation (e.g., in developing hydrogen fuel cells) or false positives (e.g., in discovering catalysts for ammonia synthesis). In this study, we elucidate the fundamental material parameters governing the stability of transition metal nitrides in acid. Such findings offer a key mechanistic understanding for rationalizing the physical origin of nitride decomposition in acid. More importantly, these insights provide a blueprint for designing and optimizing novel nitride chemistries for diverse clean energy applications.

(Figure S1), to find electronic-structure-based descriptors governing both the extent and the kinetics of nitride decomposition and ammonia formation in acid. While ionic metal nitrides (e.g., Li₃N¹³ and Mg₃N₂)¹⁴ can directly react with water through hydrolysis to generate ammonia (e.g., Li₃N + 3H₂O → 3LiOH + NH₃), transition metal nitrides are stable in air or water, but their lattice nitrogen can be activated to form ammonia through hydrogenation^{15–18} and protonation.^{3–5,19} In these processes, ammonia formation from lattice nitrogen has small barriers due to the lower electronegativity of nitrogen compared with oxygen²⁰ resulting in lower thermodynamic stability of nitrides than oxides.²¹ For the high-temperature hydrogenation of metal nitrides (e.g., 2M_xN_y + 3δH₂ → 2M_xN_{y-δ} + 2δNH₃), higher metal d orbital occupancy has been shown to lead to lower barriers for nitride hydrogenation to yield ammonia.¹⁵ However, for the room-temperature protonation of transition metal nitrides in acid (e.g., 2Fe₂N + 10H⁺ → 4Fe²⁺ + 2NH₄⁺ + H₂),¹⁹ design principles relating the kinetics of nitride dissolution and ammonia formation to the intrinsic properties of these nitrides have yet to be developed. To tackle this challenge, motivated by previous studies on the role of the ligand 2p band center in regulating the energetics of ligand vacancies^{22,23} and the surface reactivity^{23–28} of transition metal compounds, we carried out analogous investigations of the nitrogen 2p band center and decomposition energetics of nitrides using density functional theory (DFT) and X-ray emission spectroscopy (XES). Under acidic conditions, greater amounts and faster kinetics of metal ion dissolution and ammonia formation are correlated with a decreased nitrogen 2p band center with respect to the Fermi level. The lowered nitrogen 2p band center is accompanied by weakened metal–nitrogen bonds, increased metallic character, and an enhanced energetic driving force for the loss of lattice nitrogen to form ammonia. Moreover, increasing the solubility of dissolved metal cations is essential to ensure the complete conversion from nitrides to ammonia in acid by preventing surface oxide passivation.

RESULTS

Trends of nitride dissolution and ammonia formation in acid

The amounts and kinetics of metal ion dissolution and ammonia generation from nitrides were assessed by exposing nitrides to 0.1 M H₂SO₄ at room temperature. These nitrides were synthesized through solid-state nitridation.^{7,29,30} The phase purity and morphological similarity of these nitrides were confirmed by powder X-ray diffraction (PXRD, Figure S2), Raman spectroscopy (Figure S3), and scanning electron microscopy (SEM, Figure S4), respectively. The concentration of ammonium ions (produced via the reaction between ammonia and protons)³¹ was quantified by the salicylate colorimetric method^{32,33} and ¹H nuclear magnetic resonance (NMR) spectroscopy³⁴ (Figure S5). Moreover, the concentration of dissolved metal cations was measured by inductively coupled plasma mass spectrometry (ICP-MS, Figure S6). The ammonia yield, i.e., the percentage of nitrogen converted from a nitride to ammonium ions, was calculated based on the amount of nitrogen in NH₄⁺ and that in the examined nitride (Table S1). Similarly, the extent of metal ion dissolution was obtained by comparing the concentration of metal cations in acid with the amount in the nitride.

The molar concentrations of NH₄⁺ and dissolved metal ions detected after exposing nitrides to acid for 24 h decreased in the order of Fe₂N > Ni₃N > TiN > WN > VN > NbN > ZrN ~ CrN ~ Ta₃N₅ (Figure 1A, left). The amounts of NH₄⁺ detected from ZrN, CrN, and Ta₃N₅ in acid are within the experimental uncertainty (Figure S5F; Note S1). Moreover, the concentrations of NH₄⁺ found for Fe₂N and Ni₃N measured using the salicylate colorimetric method are in agreement with those from

¹Department of Materials Science and Engineering, Massachusetts Institute of Technology, Cambridge, MA 02139, USA

²Research Laboratory of Electronics, Massachusetts Institute of Technology, Cambridge, MA 02139, USA

³IEC group, Depto. Ingeniería Química y Nuclear, Universidad Politécnica de Valencia, Valencia 46022, Spain

⁴Dipartimento di Scienza dei Materiali, Università di Milano-Bicocca, Milano 20136, Italy

⁵Department of Chemical Engineering, Massachusetts Institute of Technology, Cambridge, MA 02139, USA

⁶Department of Mechanical Engineering, Massachusetts Institute of Technology, Cambridge, MA 02139, USA

⁷Lead contact

*Correspondence: yroman@mit.edu (Y.R.-L.), shaohorn@mit.edu (Y.S.-H.)

<https://doi.org/10.1016/j.joule.2022.11.011>

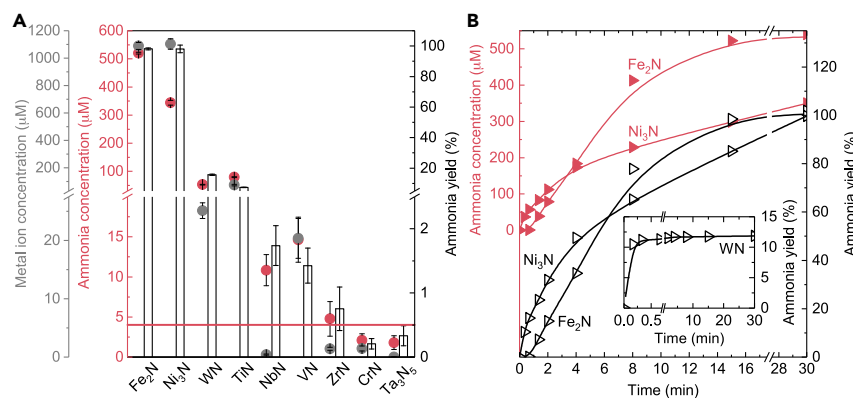


Figure 1. The extent and kinetics of nitride dissolution by exposing transition metal nitrides to acid

(A) Ammonium ion (quantified colorimetrically) and dissolved metal ion concentrations from all nitrides over 24 h in acid. For each experiment, 20 mg nitride was added into a sealed glass cell (without gas inlet or outlet) containing 300 mL 0.1 M H_2SO_4 with stirring at 800 rpm and at room temperature. Error bars represent the standard deviations of three independent measurements. The horizontal red line indicates the quantification limit of ammonia ($\sim 4 \mu\text{M}$) in this work due to the ammonia background in ambient conditions (Figure S5F; Note S1).

(B) Time-dependent ammonia formation profiles of Fe_2N , Ni_3N , and WN in acid (quantified colorimetrically). The ammonia yield is defined as the percentage of nitrogen converted from a nitride to ammonia in acid (Table S1).

^1H NMR (Figure S5F). Furthermore, the ammonia yield follows a similar trend to the concentrations of NH_4^+ and metal ions (Figure 1A, right). Notably, Fe_2N and Ni_3N had $\sim 100\%$ ammonia yields, in contrast to the lower values obtained by exposing WN ($\sim 15\%$), TiN ($\sim 7\%$), NbN ($\sim 2\%$), and VN ($\sim 2\%$) to acid.

Time-dependent measurements (Figures 1B and S7) revealed that the kinetics of ammonia formation from nitride dissolution in acid followed the trends of ammonia yields over 24 h (Figure 1A), with average rates following the order of $\text{Fe}_2\text{N} > \text{Ni}_3\text{N} > \text{WN} > \text{TiN} \sim \text{VN} \sim \text{NbN} > \text{ZrN} \sim \text{CrN} \sim \text{Ta}_3\text{N}_5$ (Figure S8). While these nitrides have different porosity levels (Figure S4) and specific surface areas (Table S1), their average dissolution rates follow a similar trend to that of the rates normalized to the specific surface areas of pristine nitrides (Figure S8). Remarkably, Fe_2N and Ni_3N exhibited fast kinetics, having complete conversion from these nitrides to ammonia within 30 min (Figure 1B), with mass-normalized initial rates as high as 0.06 and $0.04 \text{ mol}_{\text{ammonia}} \text{ h}^{-1} \text{ g}_{\text{nitride}}^{-1}$, respectively (Figure S9). Comparably fast kinetics were observed for the time-dependent dissolution of metal cations from Fe_2N and Ni_3N in acid (Figure S10). While WN showed a higher initial ammonia formation rate within the first minute of exposure to acid ($0.49 \text{ mol}_{\text{ammonia}} \text{ h}^{-1} \text{ g}_{\text{nitride}}^{-1}$, Figure S9), its ammonia formation kinetics slowed down rapidly at $\sim 12\%$ conversion, gradually reaching a plateau to $\sim 15\%$ over 24 h (Figure S7), which will be discussed in detail later.

Descriptors for nitride stability and ammonia generation in acid

Increasing the kinetics of nitride dissolution and ammonia formation in acid was correlated with a lower nitrogen 2p band center relative to the Fermi level (Figure 2A), as quantified by DFT (Figure 2B) and XES (Figures 2C and S11). The DFT-computed density of states (DOSs) of the occupied nitrogen 2p band shifted away from the Fermi level from Ta_3N_5 to NbN, VN, TiN, ZrN, and CrN, and eventually Fe_2N , Ni_3N , and WN (Figure 2B). Notably, the DFT nitrogen 2p band center,

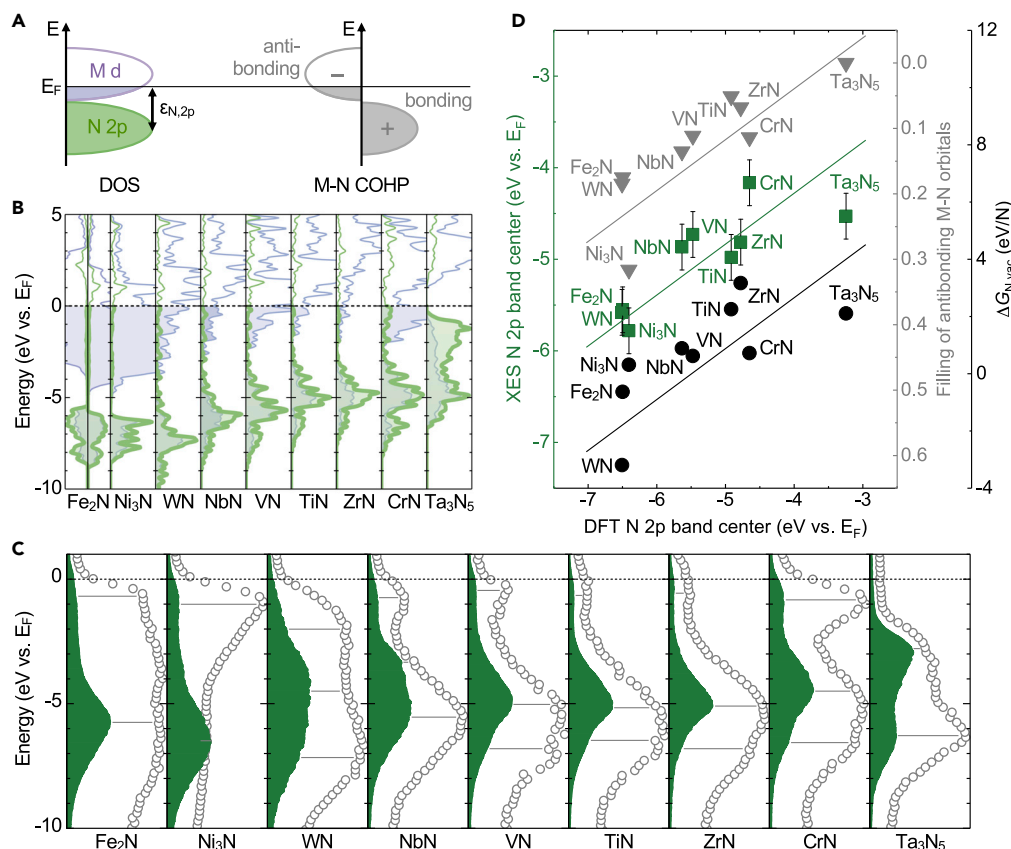


Figure 2. Electronic structures and reaction energetics of transition metal nitrides

(A) Electronic structures of transition metal nitrides represented by DOS and the bonding/antibonding nature of metal–nitrogen bonds in these nitrides indicated by their M–N COHPs.

(B) DFT-computed metal d (purple) and nitrogen 2p (green) projected DOS of transition metal nitrides. Dashed lines indicate the Fermi level.

(C) Experimental nitrogen DOS relative to the Fermi level (green, measured by N $\text{K}\alpha$ XES), quantified by aligning N $\text{K}\alpha$ XES spectra with valence band XPS spectra (dots, [supplemental experimental procedures](#)). Solid horizontal lines highlight the agreement between the hybridization features in these spectra.

(D) Trends in the XES nitrogen 2p band center (green, $r = 0.81$, where r is the Pearson correlation coefficient, [Figure S11](#)), the occupancy of antibonding M–N orbitals (gray, $r = -0.84$, [Figure S13](#)), and the energetic barrier for forming a nitrogen vacancy in transition metal nitrides (black, $r = 0.71$), as a function of the DFT nitrogen 2p band center. The DFT or XES band center was determined by the centroid of the occupied nitrogen DOS. Error bars in the XES band center represent the uncertainty in spectral alignment (~ 0.5 eV, [supplemental experimental procedures](#)).

representing the energy-weighted centroid of the nitrogen DOS (similar to our previous work²⁶ on the oxygen 2p band center of transition metal oxides), was lowered due to increased metal d electron filling ([Figures 2B and S12](#)). Moreover, the DFT nitrogen 2p band center, along with the metal–nitrogen hybridization features in the computed DOS, was in good agreement with the experimental nitrogen DOS ([Figures 2C and 2D](#)), quantified by N $\text{K}\alpha$ XES and aligned to the Fermi level with valence band X-ray photoelectron spectroscopy (XPS) based on a method developed previously^{35,36} ([Figure S11; supplemental experimental procedures](#)). Such hybridization features in N $\text{K}\alpha$ XES from lower to higher photon energies can be attributed to the bonding, non-bonding, or antibonding orbitals of metal–nitrogen bonds, respectively (similar to the order of orbitals observed for transition metal oxides),^{35,36} indicating that N $\text{K}\alpha$ XES primarily reflects the ground-state DOS of these nitrides. Additional support for the DFT-based analysis is found in the agreement between the experimental and DFT-relaxed structures of the nitrides assessed in this work ([Figure S2; Table S2](#)). While XES provides a more direct quantification of

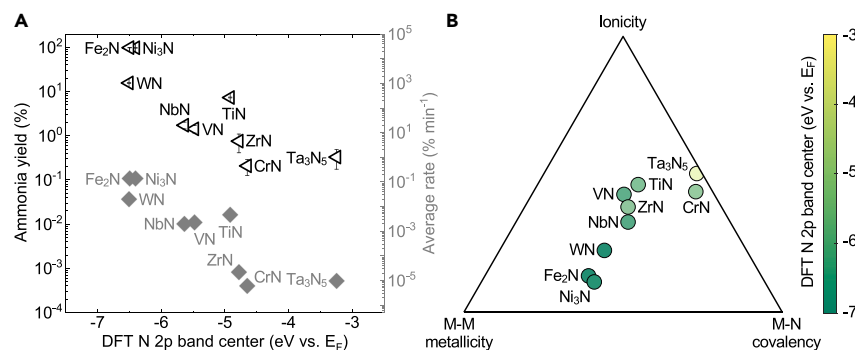


Figure 3. Nitrogen 2p band center as a descriptor for dissolution kinetics and bonding character

(A) Trends in the ammonia yields ($r = -0.82$, where r is the Pearson correlation coefficient) and the average rates of ammonia formation from nitrides over 24 h in acid (quantified by the colorimetric method, $r = -0.87$), as a function of the DFT nitrogen 2p band center. These average rates were estimated based on the area under the curve in the time-dependent ammonia formation profiles (Figure S7). Error bars in the ammonia yields represent the standard deviations of three independent measurements. The nitrogen 2p band center was determined by the centroid of the DFT-computed occupied nitrogen DOS (Figure 2B).

(B) Metallicity, ionicity, and covalency of metal nitrides plotted on the van Arkel-Ketelaar diagram based on the DFT-computed electron density (supplemental experimental procedures). The values of these quantities were normalized by the maximum of each quantity among all nitrides examined in this work, and thus this van Arkel-Ketelaar diagram shows the relative metallic-ionic-covalent bonding character of such nitrides (instead of their absolute values).

the electronic structure of transition metal compounds than DFT.^{35,36} XES measurements are also more resource intensive. In contrast, DFT-computed electronic-structure-based descriptors can be more suited for materials discovery, e.g., through high-throughput virtual screening, owing to the continued development of computational materials databases.³⁷ Overall, the examination of both DFT- and XES-based descriptors in this work can provide a rigorous co-validation of simulations and experiments.

Lowering the nitrogen 2p band center relative to the Fermi level weakens metal–nitrogen bonds (Figure 2D) and increases labile metal–metal interactions in nitrides (Figure 3B), associated with faster kinetics of nitride decomposition in acid (Figures 3A and S11D). First, the weakening of metal–nitrogen bonds when the Fermi level is lifted up with respect to the nitrogen 2p band is supported by the crystal orbital Hamilton population (COHP) analysis (Figure S13). COHPs show the orbital overlaps and, therefore, the bonding ($\text{COHP} > 0$) or antibonding ($\text{COHP} < 0$) nature of electronic orbitals in chemical bonds.³⁸ The occupancy of antibonding orbitals in metal–nitrogen bonds can then be quantified by integrating the M–N COHPs of nitrides from the bottom of the valence band to the Fermi level³⁹ (Figure S13). Thus, a lower nitrogen 2p band center relative to the Fermi level leads to more filled antibonding states (Figure 2D). Fe_2N and Ni_3N , featuring the lowest nitrogen 2p band center, have the most occupied antibonding M–N orbitals and the weakest metal–nitrogen bonds, consistent with their fastest kinetics of nitride dissolution in acid (Figures 1B and 3A). Second, the increased occupancy of antibonding states with dominantly metallic character can also result in an increased contribution of labile metal–metal bonds in these nitrides. The contribution of metal–metal interactions near the Fermi level of Fe_2N and Ni_3N is the highest among all nitrides examined here, as indicated by their M–M COHPs (Figure S13B). To further support this argument, the metallic-ionic-covalent character of these metal nitrides was quantified based on the DFT-computed electron density⁴⁰

(supplemental experimental procedures) and plotted on the van Arkel-Ketelaar diagram.⁴¹ Lowering the nitrogen 2p band relative to the Fermi level was found to lead to a more metallic character for such nitrides (Figure 3B), and thus, Fe₂N and Ni₃N have the strongest metallic character. Notably, Fe₂N and Ni₃N also have the most reactive metal–metal bonds, as late transition metals (e.g., Fe) have been shown to have weak metallic bonds and fast dissolution in acid due to their high d shell filling.⁴² Thus, Fe₂N and Ni₃N have the highest contribution of labile metal–metal interactions among their chemical bonds, accounting for their fastest dissolution kinetics in acid. In contrast, no strong correlations exist between the formation energetics of transition metal nitrides and their dissolution kinetics in acid (Figure S14), highlighting the role of electronic-structure-based descriptors such as the nitrogen 2p band center in governing the stability of nitrides in acid.

Lowering the nitrogen 2p band center of transition metal nitrides relative to the Fermi level is also correlated with a decreased barrier for forming nitrogen vacancies and an increased driving force for the protonation of lattice nitrogen to produce ammonium ions, where a lattice nitrogen ion reacts with protons to form NH₄⁺ (i.e., N_{lattice} + 4H⁺ → □³⁺ + NH₄⁺, having □ as a vacancy site created after the removal of the nitrogen anion). The energetic barrier of such a protonation reaction differs by the energy penalty for generating a nitrogen vacancy in nitrides ($\Delta G_{N\ vac}$). Lowering the nitrogen 2p band center relative to the Fermi level reduced $\Delta G_{N\ vac}$ by ~7 eV across all assessed nitrides (Figure 2D), indicating an increased thermodynamic driving force for the protonation step. This lowered penalty can be in part rationalized by the weakening of metal–nitrogen bonds due to the decreased nitrogen 2p band center relative to the Fermi level (Figures 2D and 3B), as the breaking of metal–nitrogen bonds is involved in the protonation reaction. This reduced penalty can also be related to a lowered charge-transfer barrier from transition metal nitrides to protons (Figure S15), as such electron transfer from the highest occupied orbitals of nitrides to the empty orbital of protons is crucial for forming nitrogen–hydrogen covalent bonds during the protonation and loss of lattice nitrogen sites in acid. Other energetics, such as those relevant to charge redistribution in nitrides after creating vacancies (similar to what has been shown for oxides),^{25,26,43,44} can also potentially influence the trends in $\Delta G_{N\ vac}$ (Figure 2D). Future work is required to resolve different competing energetics during vacancy formation in transition metal nitrides, which can be essential for further understanding their stability trends.

Effect of surface oxidation and ion solubility on nitride dissolution

Fe₂N and Ni₃N, with the lowest nitrogen 2p band center, were the most oxidized on the surface among all examined nitrides (Figure S16). This trend can be rationalized by the increased energetic driving force for the oxidation of metal nitrides, e.g., M_xN_y + (z/2)O₂ → M_xO_z + (y/2)N₂,⁴⁵ due to the weak metal–nitrogen bonds in Fe₂N and Ni₃N. This argument is in agreement with a recent work on metal carbides reporting that stronger metal–carbon bonds result in carbides that are harder to oxidize.⁴⁶ Moreover, the surface and bulk metal valence states in Fe₂N and Ni₃N were quantified by metal 2p XPS and metal K-edge X-ray absorption near edge structure (XANES), respectively. While Fe²⁺ and Fe³⁺ surface species (e.g., FeO and Fe₂O₃) were observed for pristine Fe₂N (Figure S17B), the bulk Fe oxidation state was estimated to be +1.5, as expected for Fe₂N (Figure S17C). Similarly, while the pristine Ni₃N surface is composed of Ni⁺ and Ni²⁺ (Figure 4B), indicating the presence of NiO species, the bulk Ni oxidation state of as-synthesized Ni₃N is close to +1, as expected for Ni₃N (Figure 4C). After exposing these nitrides to acid for 10 min, where ~81 and ~71 wt % of Fe₂N and Ni₃N reacted, respectively, their surface and bulk metal oxidation states remained unchanged compared with those of

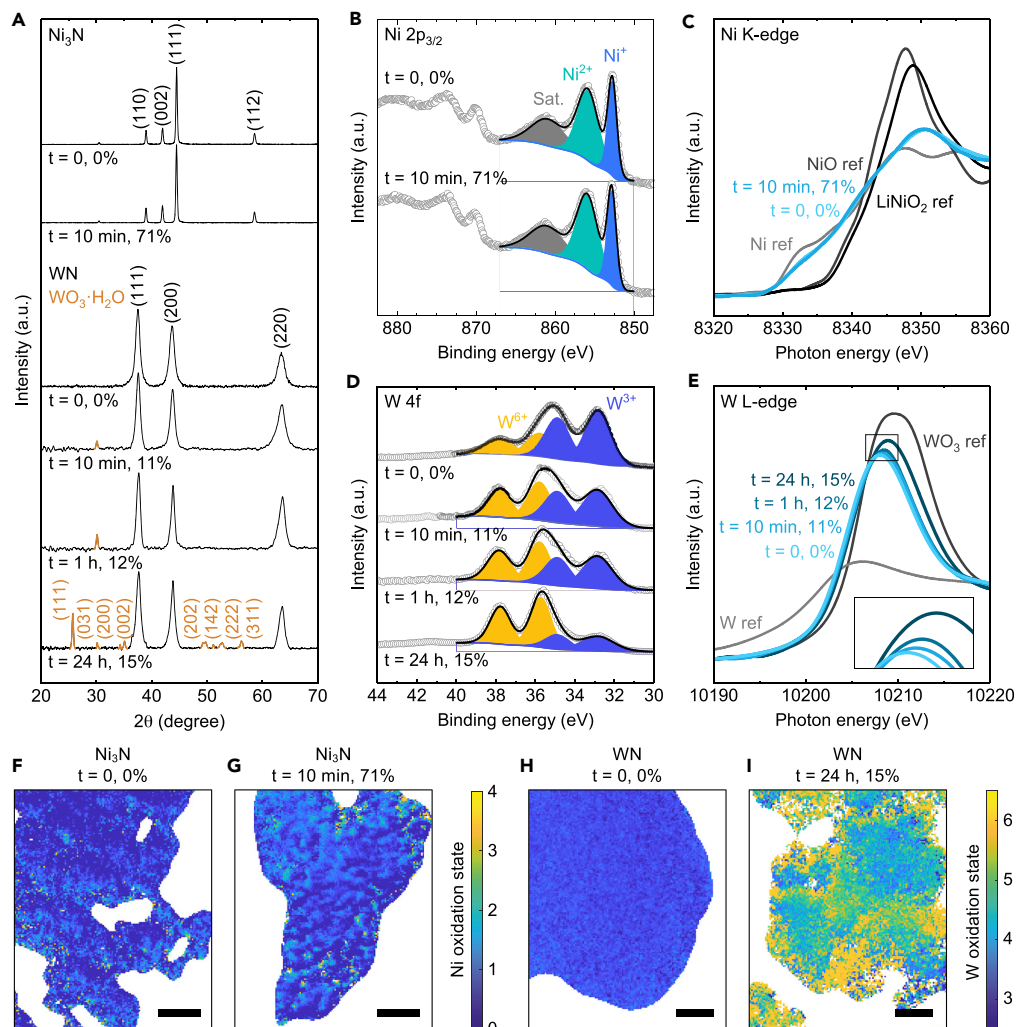


Figure 4. Influence of the solubility of dissolved metal cations on nitride dissolution kinetics

(A) PXRD of Ni_3N and WN before and after exposure to acid, labeled by the exposure time and the percentage of conversion from these nitrides to ammonia. All peaks for Ni_3N after exposure to acid can be assigned to the hexagonal Ni_3N phase ($\text{P}6_3\text{2}2$, $a = b = 0.46 \text{ nm}$, $c = 0.43 \text{ nm}$, Figure S1). For WN after exposure to acid, the major peaks can be assigned to the cubic rocksalt WN phase ($\text{Fm}\bar{3}\text{m}$, $a = b = c = 0.41 \text{ nm}$, Figure S1), while a secondary phase (orange peaks) exists and matches with the standard PXRD pattern of the orthorhombic $\text{WO}_3 \cdot \text{H}_2\text{O}$ phase ($\text{Pmn}b$, $a = 0.52 \text{ nm}$, $b = 1.07 \text{ nm}$, $c = 0.51 \text{ nm}$, Figure S19A).

(B) Ni 2p XPS spectra of Ni_3N before and after exposure to acid. The $2\text{p}_{3/2}$ peaks from low to high binding energies correspond to Ni^+ (852.8 eV), Ni^{2+} (855.9 eV), and satellite peaks (861.0 eV), respectively.⁴⁷

(C) Ni K-edge XANES spectra of Ni_3N before and after exposure to acid.

(D) W 4f XPS spectra of WN before and after exposure to acid. The two sets of $4\text{f}_{7/2}$ and $4\text{f}_{5/2}$ doublets from low to high binding energies correspond to W^{3+} (32.8 and 34.9 eV) and W^{6+} (35.7 and 37.8 eV), respectively.^{48,49}

(E) W L-edge XANES spectra of WN before and after exposure to acid.

(F and G) Ni oxidation state maps of Ni_3N before (F) and after exposure to acid for 10 min (G). Scale bars, 1 μm .

(H and I) W oxidation state maps of WN before (H) and after exposure to acid for 24 h (I). Scale bars, 2 μm . Additional two-dimensional metal oxidation state maps are provided in Figure S21.

pristine nitrides (Figures 4B, 4C, S17B, S17C, S18A, and S18B), consistent with the observation that Fe_2N and Ni_3N remained crystalline and phase-pure after exposure to acid (Figures 4A and S17A).

WN, having a comparable nitrogen 2p band center to Fe_2N and Ni_3N , was shown to have fast kinetics for the first minute of exposure to acid, after which its dissolution

rate was reduced significantly (Figure 1B). The observed change in nitride dissolution kinetics can be attributed to the formation of acid-stable oxides on the surface of WN upon the initial dissolution of tungsten cations in acid. This point is supported by the new peaks in the PXRD patterns of WN after exposure to acid (Figure 4A), with steady growth in intensities after the exposure time increased from 10 min, 1 h, to 24 h, which can be indexed to tungsten oxide hydrate ($\text{WO}_3 \cdot \text{H}_2\text{O}$, Figure S19A). This result is corroborated by the changes in the W L-edge XANES spectra of WN after exposure to acid, showing a positively shifted absorption edge and increased white line intensity (Figure 4E), and the formation of $\text{WO}_3 \cdot \text{H}_2\text{O}$ is supported by the linear combination analysis (Figures S18C–S18E). Further support comes from the W 4f XPS spectra (Figure 4D), where the relative intensity of doublet peaks corresponding to W^{6+} ions in WO_3 increased markedly at the expense of W^{3+} doublet peaks from WN. These observations are in agreement with the different aqueous solubility of metal cations at acidic pHs, as indicated by the Pourbaix diagrams (Figure S20). Tungsten ions, formed after the exposure of WN to acid, are insoluble at acidic pHs, leading to the generation of acid-stable oxide phases (e.g., WO_3 , Figure S20A). In contrast, iron and nickel ions are soluble in acid (Figures S20B and S20C), inhibiting the passivation of Fe_2N and Ni_3N particles by corresponding oxide phases after the dissolution of these two metal nitrides.

The metal-dependent passivation of nitrides by acid-stable oxides was visualized by using synchrotron full-field transmission X-ray microscopy (TXM, Figures 4F–4I and S21). Negligible changes were found in the TXM maps of Fe_2N (Figure S21A) and Ni_3N (Figures 4G and S21B) at ~81% and ~71% conversion from these nitrides to ammonia, respectively. In contrast, in the TXM maps of WN, the tungsten oxidation states in the surface regions were shown to increase after 10 min and 1 h in acid (Figure S21C), and large oxide particles (e.g., $\text{WO}_3 \cdot \text{H}_2\text{O}$) became visible after 24 h in acid with ~15% conversion from WN to ammonia (Figure 4I). These results are in agreement with the increasingly reduced surface N/(N+O) ratios, as well as the higher tungsten oxidation states on the surface than in bulk, estimated from W 4f XPS and W L-edge XANES, respectively (Figure S19C).

The formation of acid-stable oxide phases is not limited to WN and has essential implications on the extent and kinetics of nitride dissolution and ammonia formation in acid. For WN, the formation of tungsten oxide phases from dissolved tungsten cations can explain why the percentage of detected tungsten cations is much lower than that of quantified ammonia from the dissolution of WN in acid (Figure S10A), as large particles were filtered out of the acidic solutions before the ICP-MS quantification. Similar to WN, NbN had almost no niobium cations in acid after its dissolution (Table S3), which can be rationalized by the low solubility of niobium ions owing to the large thermodynamic driving force for forming Nb_2O_5 from niobium ions in acid (Figure S20K). In addition, although titanium cations are similarly insoluble in acid (Figure S20J), TiN was less passivated by TiO_2 than NbN by Nb_2O_5 (Table S3), which explains why TiN had more ammonia formation and nitride dissolution (Figure 3), even though it has a higher N 2p band center and thus stronger metal–nitrogen bonds than NbN (Figure 2). Furthermore, the result that NbN was more passivated by acid-stable oxides than TiN agrees with their time-dependent dissolution profiles (Figure S7), where the kinetics of NbN slowed down rapidly after the first minute, while the dissolution of TiN was slow yet steady in acid. Overall, these observations highlight that the influence of oxidized phases on nitride dissolution kinetics in acid is not governed predominantly by the initial surface oxidation of nitrides in the air (Figure S16), but, instead, by the solubility of dissolved metal ions at acidic pHs.

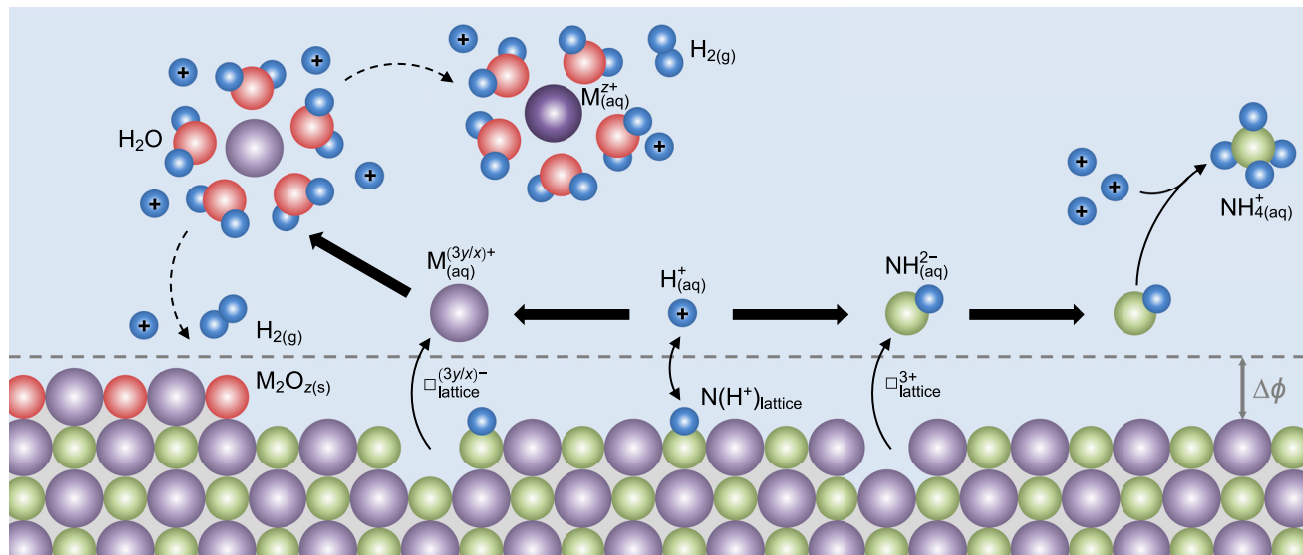


Figure 5. Proposed reaction scheme for nitride dissolution and ammonia formation in acid

The solvation structure of aqueous ions is not shown unless water explicitly participates in the corresponding reactions. $\Delta\phi$ represents the potential difference across the double layer. Color scheme: metal, purple; N, green; O, red; H, blue.

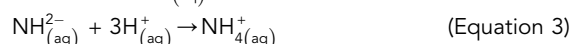
(Figure S20). Such results show the complex interplay between nitride decomposition and oxide formation in governing the kinetics of nitride dissolution and ammonia formation in acid.

Mechanistic insights into nitride dissolution in acid

The design principles for nitride stability and ammonia generation can provide critical mechanistic insights into the decomposition of transition metal nitrides in acid. Given the key role of the nitrogen 2p band center in controlling nitride dissolution kinetics by modulating metal–nitrogen bond strength (Figures 2 and 3) and the protonation of lattice nitrogen sites (Figure S15), we propose a possible protonation-promoted pathway for nitride dissolution in acid (Figure 5). It has been widely conceived that the decomposition of inorganic solids in aqueous solutions is facilitated by the protonation of their lattice ligand sites.^{25,50–52} For example, the protonation of lattice oxygen in transition metal oxides can polarize and weaken adjacent metal–oxygen bonds, facilitating their dissolution in acid.^{25,51} Likewise, protonating lattice nitrogen in silicon nitrides can increase the electrophilicity of neighboring silicon sites to render the sites more accessible for nucleophilic attack by water.⁵² Motivated by such examples^{25,51,52} and the theory of solid dissolution in acid proposed by Crundwell,^{53,54} we hypothesize that the decomposition of metal nitrides in acid begins with the protonation of lattice nitrogen to generate activated lattice nitrogen species⁵⁵ (Figure 5),



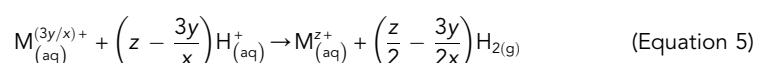
which polarizes adjacent metal–nitrogen bonds and makes metal and nitrogen ions less bonded to each other. The activated species can depart from the surface of nitrides by breaking metal–nitrogen bonds and diffusing into the bulk solutions and then further react with protons to generate ammonium ions:



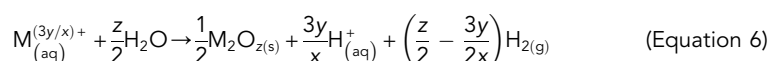
where \square represents the vacancy generated after the removal of lattice ions. Simultaneously, transition metal cations can leave the surface by breaking metal–nitrogen bonds, become solvated by water, and diffuse into the bulk solutions (Figure 5):



These metal ions can potentially be further oxidized into cations with a higher oxidation state if soluble,



consistent with the product quantification for Fe_2N by Fowler (i.e., $2\text{Fe}_2\text{N} + 10\text{H}^+ \rightarrow 4\text{Fe}^{2+} + 2\text{NH}_4^+ + \text{H}_2$).¹⁹ Such dissolved metal cations can also transform into acid-stable oxide phases if having low solubility,



which agrees with the formation of oxide phases (e.g., $\text{WO}_3 \cdot \text{H}_2\text{O}$) for WN in acid (Figure 4).

Given our proposed reaction scheme (Figure 5; Equations 1, 2, 3, 4, 5, and 6), we can further derive the kinetic model for nitride dissolution in acid using the theory of solid dissolution proposed by Crundwell^{53,54} and compare our theoretical model with experiments. We assume that the breaking of metal–nitrogen bonds is the hardest process (i.e., Equation 2 for ammonia formation and Equation 4 for metal ion dissolution), as metal–nitrogen bond strength essentially governs dissolution kinetics (Figures 2 and 3). Notably, since Equations 2 and 4 create net charges in vacancies due to the detachment of ions, such charges can be either mobile or captured by surface states and dangling bonds.⁵³ More importantly, the migration of charged ions between the surface of nitrides and the bulk solutions can give rise to a potential difference across the double layer⁵³ (Figure 5), and this potential drop, in turn, influences the reaction rates of those steps involving the transfer of charged ions at the solid-liquid interface (e.g., Equations 1, 2, and 4). Considering the charged solid-liquid interface, even though ammonia formation and metal ion dissolution appear to be two independent, parallel processes, they are kinetically coupled because their rates depend on the potential difference across the double layer. Thus, steady-state dissolution is established when the rates of ammonia formation and metal ion dissolution are proportional to the stoichiometry of nitrides (i.e., M_xN_y):



where r denotes the reaction rate. After considering such congruent, stoichiometric dissolution of transition metal nitrides, we can derive their decomposition rates in acid (Note S2) and compare our theoretical model with experimental results. Specifically, the key role of protons is corroborated by the negligible amounts of ammonia and dissolved metal cations detected after exposing the most reactive Fe_2N and Ni_3N to pure water (Figure S22). Further support comes from the pH-dependent kinetics of Ni_3N in acid, where decreasing pH led to faster dissolution kinetics with a reaction order of -0.2 with respect to pH (Figure S23), in reasonable agreement with our kinetic model that gives rise to a reaction order of -0.25 with respect to pH (Note S2). Nevertheless, it is crucial to emphasize that currently, we cannot exclude alternative reaction mechanisms that potentially result in similar pH dependence, and broadly speaking, our findings represent the first step toward understanding nitride

dissolution in acid. For instance, future studies are required to systematically elucidate the oxidation of dissolved metal cations in acid (Equations 5 and 6), e.g., by accurately quantifying the formation of hydrogen gas and the product distribution of oxidized species.¹⁹ In addition, the descriptor-centered approach should be extended in future work to unravel the physical principles behind the solubility of dissolved metal ions in acid, as currently, only a preliminary understanding exists for the crystallization processes of different transition metal oxides in aqueous solutions.^{56,57} Given the complex interplay between nitride dissolution, ammonia generation, metal cation oxidation, and oxide formation, we must continue to refine and extend the stability design principles of transition metal nitrides in acid.

DISCUSSION

In this work, we report the nitrogen-2p-band-center-dependent energetics and kinetics of transition metal nitride dissolution and ammonia generation in acid. Notably, we show that lowering the nitrogen 2p band center of transition metal nitrides leads to weakened metal–nitrogen bonds and increased labile metal–metal interactions, providing a large driving force for protonating lattice nitrogen and forming nitrogen vacancies to decompose nitrides and generate ammonia in acid. In addition, having high solubility of dissolved metal cations ensures the complete conversion from nitrides to ammonia by preventing surface oxide passivation. Such design principles can be extended to rationalize the stability trends of well-studied nitride chemistries for electrocatalysis in acid. For instance, Mo₂N has fast dissolution in acid,³ which can be explained by its weak Mo–N bonds similar to the W–N bonds in W-based nitrides due to the comparable electronegativities of Mo and W.⁵⁸ Moreover, the stability of Mo-based nitrides in acid is enhanced by increasing the nitrogen content from Mo₂N to MoN,⁵⁹ which oxidizes the Mo ions, moves the Fermi level closer to the N 2p band center, and leads to stronger Mo–N bonds. Thus, nitrogen-rich Mo-based nitrides (e.g., Co_{0.6}Mo_{1.4}N₂)⁶⁰ and Fe_{0.8}Mo_{1.2}N₂)⁶¹ can be used to stabilize late transition metal cations in nitrides for oxygen reduction in acid. These observations support the power of stability design principles based on the bulk electronic structure of transition metal compounds in capturing their surface energetics and kinetics in a wide chemical space, similar to what has been shown in our prior work on transition metal oxides.^{25,26} Nevertheless, in this work, we focus on nitrides composed of early 3d to 5d or late 3d transition metals since these metals tend to form synthetically accessible binary⁶² and ternary⁴⁰ nitrides. Thus, caution is needed when directly extrapolating the stability design principles reported in this study for novel nitride compositions comprising late 4d or 5d transition metals.⁶³ More importantly, apart from the surface passivation of nitrides by acid-stable oxides, in electrocatalysis, electrochemically induced surface transformations (e.g., the formation of oxide shells)⁶⁴ can occur on transition metal nitride catalysts, particularly under oxidizing potentials. Such oxidized phases might not be catalytically active and thus block the active sites of their parent nitrides. However, for certain nitrides, these oxide⁶⁵ or oxynitride⁶⁶ species have been proposed to boost the catalytic activity by forming highly active surface reaction sites. Therefore, this work should be extended in future studies to understand the formation of electrochemically induced oxidized phases on transition metal nitrides, e.g., by leveraging the operando spectroscopic⁶⁷ and microscopic characterization⁶⁸ of nitride-electrolyte interfaces.

These design principles of nitride stability and ammonia generation in acid can be leveraged to design new nitride chemistries for diverse acidic applications. For instance, the intrinsic stability of nitride catalysts for electrochemical oxygen^{7,8}

or nitrogen reduction^{3–5} in acid can be enhanced by designing nitride chemistries with increased nitrogen 2p band relative to the Fermi level. In contrast, lowering the nitrogen 2p band center relative to the Fermi level can give rise to transition metal nitrides with facile, complete ammonia formation kinetics in acid, providing novel opportunities for distributed, on-demand ammonia generation,⁶⁹ especially if, through future studies, nitride synthesis can be achieved utilizing earth-abundant nitrogen sources (e.g., dinitrogen and nitrates) and metal oxide or metal salt precursors (recovered from the dissolved metal cations in acid). Notably, the optimization of the nitrogen 2p band center of transition metal nitrides can be realized through rational metal substitution⁷⁰ in these nitrides. Specifically, to boost nitride stability in acid (e.g., for proton exchange membrane fuel cells), electropositive heterometals can possibly be substituted in existing nitride catalysts to form more nitrogen-rich, mixed ionic-covalent nitrides (presumably with higher nitrogen 2p band). On the contrary, to promote the ammonia formation kinetics from exposing nitrides to acid (e.g., for distributed, on-demand ammonia production), electronegative metal ions can be potentially introduced in known chemistries to generate more nitrogen-poor, metallic nitrides (presumably with lower nitrogen 2p band). Such a strategy based on the chemistry, electronic structure, and bonding characteristics of transition metal nitrides (Figure 3B) is supported by the similar metallic-ionic-covalent character of 54 synthetically accessible ternary transition metal nitrides discovered in a recent study.⁴⁰ Decreasing the electronegativity of substituents has been found to reduce neighboring nitrogen anions and oxidize the parent metal, which can be compensated by excess nitrogen and give rise to the formation of nitrogen-rich, mixed ionic-covalent nitrides.⁴⁰ In contrast, increasing the electronegativity of heterometals has been proposed to oxidize adjacent nitrogen anions, redistributing more electron density to metal–metal bonds (instead of metal–nitrogen bonds) and leading to the creation of nitrogen-poor, metallic nitrides.⁴⁰ The stability design principles of transition metal nitrides in acid shown in this work can potentially serve as a blueprint to further establish generalized activity⁹ and synthesizability descriptors⁴⁰ for substituted multinary nitrides. For example, electrochemical nitrogen reduction to ammonia on transition metal nitrides has been proposed to operate via the nitrogen-vacancy-mediated Mars–van Krevelen mechanism.^{2,9–12} Therefore, reducing the nitrogen 2p band center of nitrides can potentially lower the catalytic reaction barrier if the vacancy formation process is rate limiting but increase this energetic barrier if, instead, the replenishment of lattice nitrogen sites is rate determining. As nitrides represent an exciting, yet largely unexplored chemical space compared with other chemistries (e.g., oxides),^{21,40} from a broad perspective, we aim to leverage emerging data-driven toolsets^{37,71} in future work to co-optimize the synthesizability, activity, and stability of nitrides across a wide chemical space for diverse acidic applications including electrocatalysis and beyond.

EXPERIMENTAL PROCEDURES

Resource availability

Lead contact

Further information and requests for resources and materials should be directed to and will be fulfilled by the lead contact, Yang Shao-Horn (shaohorn@mit.edu).

Materials availability

This study did not generate new unique materials.

Data and code availability

This study did not generate any datasets.

Materials and methods

Materials synthesis

All reagents were commercially available and utilized as received. All nitrides were prepared through the nitridation of metal oxide or metal salt precursors or the renitridation of commercial metal nitride powders. In a typical synthesis, 0.5 g precursor was loaded into a ceramic boat, nitridized at 350°C–900°C with a heating rate of 2°C min⁻¹ in a flow of NH₃ (100 cm³ min⁻¹, ultra-high purity, Airgas) for 1–20 h, cooled to room temperature, and passivated for 30 min with a 1% O₂/99% N₂ mixture (100 cm³ min⁻¹, Airgas). The passivated sample was quickly removed from the ceramic boat and further placed in a glass vial before characterization and testing. The complete list of nitrides, precursors, nitridation temperatures, and time is: Fe₂N, Fe₂O₃ (Sigma-Aldrich), 500°C, 6 h; Ni₃N, NiCl₂ hexahydrate (Sigma-Aldrich), 350°C, 6 h; WN, WO₃ (Sigma-Aldrich), 700°C, 3 h; TiN, TiN (Strem Chemicals), 900°C, 3 h; NbN, Nb₂O₅ (Sigma-Aldrich), 750°C, 11 h; VN, VN (Strem Chemicals), 350°C, 1 h; ZrN, ZrN (Strem Chemicals), 900°C, 20 h; CrN, Cr₂O₃ (Sigma-Aldrich), 770°C, 14 h; Ta₃N₅, Ta₂O₅ (Sigma-Aldrich), 900°C, 20 h.

Characterization

PXRD measurements for all examined metal nitrides except Fe₂N were performed using a Bruker Advance II diffractometer equipped with a $\theta/2\theta$ Bragg-Brentano geometry and Ni-filtered Cu K α radiation ($\lambda = 1.5418 \text{ \AA}$). Due to the strong fluorescence from Fe-containing samples when using a Cu X-ray source, PXRD pattern of Fe₂N was collected using a Bruker D8 general area detector diffraction system equipped with a two-dimensional area detector and Co K α radiation ($\lambda = 1.7902 \text{ \AA}$). PXRD patterns of as-synthesized nitrides were collected in a step scan mode with a step size of 0.02°, a step time of 1 s per step, and a scan range of 20°–90°. PXRD patterns of acid-treated nitrides were collected in a step scan mode with a step size of 0.04°, a step time of 30 s per step, and a scan range of 20°–70°. XPS measurements were conducted using a Thermo Scientific Nexsa X-ray photoelectron spectrometer system with monochromatic Al K α radiation (1,486.6 eV) and a low-energy flood gun as a neutralizer. The binding energy of the C 1s peak at 284.8 eV was used as a reference for charge correction, and the Fe 2p, Ni 2p, and W 4f core-level spectra were fitted using Gaussian-Lorentzian peaks (30% Lorentzian) after Shirley-type background subtraction. The specific surface area of each nitride was determined using a Quantachrome ChemBET Pulsar system from a single-point Brunauer-Emmett-Teller analysis after 12 h outgassing at 150°C in an N₂ atmosphere. Raman spectra for all nitrides except CrN were measured using a Horiba LabRAM HR microscope Raman spectrometer system with 532 and 632 nm laser excitation. For CrN, its Raman spectrum was measured using a Renishaw inVia reflex Raman microscope with 785 nm laser excitation. SEM images were collected using a Zeiss Merlin high-resolution scanning electron microscope at 5 kV.

Exposing metal nitrides to acid

The exposure of metal nitrides to acidic solutions was assessed by adding 20 mg nitride powders into a sealed glass cell (without gas inlet or outlet) containing 300 mL 0.1 M H₂SO₄ (Sigma-Aldrich, ACS reagent) with stirring at 800 rpm. Deionized (DI) water (18.2 MΩ cm at 25°C) was used from a Millipore Milli-Q water purification system and was freshly prepared just before use. For each liquid sample, 3 mL solution was taken, filtered, and stored for quantification. For each solid sample, nitride powders after exposure to acid for a specific amount of time were filtered, washed with DI water, dried in the air, and stored for further characterization.

Ammonia quantification

Ammonia concentrations were colorimetrically quantified using the salicylate method,^{32,33} which has been modified from the approach reported previously.^{72,73} This method only works for neutral/alkaline samples, because at acid pHs, sodium salicylate precipitates out of the solutions as salicylic acid. Thus, given that the sample solutions were highly acidic, for each sample, 2.5 mL solution was neutralized with 2.85 mL 0.2 M KOH (Sigma-Aldrich, ACS reagent) just prior to the quantification to reduce potential ammonia loss via evaporation in alkaline conditions.

Three reagent solutions were prepared for the salicylate method, i.e., a salicylate catalyst solution (S1), an alkaline citrate solution (S2), and an alkaline hypochlorite solution (S3). Specifically, S1 was prepared by dissolving sodium salicylate (EMSURE Millipore, for analysis) and sodium nitroprusside dihydrate (EMSURE Millipore, for analysis) in DI water to obtain a 2.75 M sodium salicylate and 0.95 mM sodium nitroprusside solution. S2 was prepared by dissolving sodium citrate dihydrate (EMSURE Millipore, for analysis) and KOH in DI water to obtain a 340 mM sodium citrate dihydrate and 465 mM KOH solution. S3 was prepared by mixing 10 vol. % of commercial 5% sodium hypochlorite aqueous solution (ACROS Organics) with 90 vol. % of S2. S1 and S3 were always freshly prepared just prior to the quantification and never stored for more than 1 day, while S2 was prepared in advance and stored at room temperature. In addition, when not in use, S1 was always kept in an opaque dark bottle.

Apart from these reagent solutions, a set of calibration standards was prepared just before analyzing the samples. In order to get these calibration standards as similar as possible to the actual samples, the solvent for these calibration standards was prepared by mixing 0.1 M H₂SO₄ with 0.2 M KOH in the same volume ratio used for neutralizing the samples. A mother solution was further prepared by dissolving ammonium chloride (EMSURE Millipore, for analysis) in the prepared solvent. Then, a set of calibration standards was prepared by diluting the mother solution with the prepared solvent following different volume ratios, where a blank standard (i.e., a solvent with no mother solution) was always included.

For the colorimetric quantification of each sample, 5 mL neutralized solution was mixed vigorously with 600 µL S1 and 1 mL S3 in the dark, and this solution was stored in the dark. After color development for 1 h, the ultraviolet-visible (UV-vis) spectra of the stored solutions were measured using a Thermo Scientific GENESYS 180 UV-vis spectrophotometer, where the blank standard was used as the blank solution and reference solution for UV-vis measurements. All UV-vis spectra were collected from 850 to 350 nm, with a step size of 0.5 nm and a speed of 5 nm s⁻¹. After all measurements, calibration curves were obtained by plotting the absorbance at 650 nm (A_{650}) of the calibration standards versus their ammonia concentrations, and the ammonia concentrations in sample solutions were further determined by projecting their A_{650} values following the linear correlations (fitted with a zero y-intercept) in the calibration curves. While the presence of Fe ions can potentially influence ammonia quantification via the salicylate method due to the formation of Fe(OH)₃ precipitates and Fe(III) salicylate complexes,³² the concentration of Fe³⁺ ions in our experiments by exposing Fe₂N to acid is too low to give rise to any interference, as supported by our control experiment. Specifically, by manually adding up to 280 ppm (i.e., ~5.0 mM) Fe³⁺ cations into the calibration standards, we found that the absorbance of Fe(OH)₃ precipitates and Fe(III) salicylate complexes at 400–500 nm has negligible influence on the quantification peak at 650 nm (Figure S5C). Given that the maximum possible concentration of Fe ions from the complete decomposition of Fe₂N in our experiments is estimated to be ~59.2 ppm (i.e., ~1.06 mM, Table S1), the presence

of Fe-containing precipitates and complexes does not influence the ammonia quantification via the salicylate method.

In addition to the colorimetric method, ammonia concentrations were also quantified using ^1H NMR. In a typical NMR experiment, an internal standard was first prepared by dissolving dimethyl sulfone (Sigma-Aldrich, standard for quantitative NMR) in DI water. Then, each NMR sample was prepared by mixing 1 mL sample solution with the required volume of internal standard so that the internal standard concentration was within the same order of magnitude as the estimated concentration of ammonia in the sample solution (based on the colorimetric method). The NMR sample was further mixed thoroughly with 5 μL concentrated hydrochloric acid (Sigma-Aldrich, ACS reagent, 37%) and 100 μL acetonitrile- d_3 (Sigma-Aldrich, ≥ 99.8 at. % D) in order to ensure complete homogenization prior to introducing the sample into an NMR tube. All NMR spectra were collected at 25°C using a three-channel Bruker Avance Neo spectrometer operating at 500.34 MHz. The spectrometer is equipped with a 5 mm liquid-nitrogen cooled Prodigy broadband observe cryoprobe and runs in full-automation mode with a SampleXpress 60 sample changer. NMR measurements were conducted using the ^1H water suppression method based on 1D excitation sculpting using 180° water-selective pulses with a T_1 relaxation time of 20 s, and the number of scans was selected so that the signal-to-noise ratio of NH_4^+ signals was greater than 250. All NMR spectra were processed using MestReNova by the baseline correction of free induction decay, Fourier transformation, and phasing. All chemical shifts were referenced to tetramethylsilane, using a virtual reference provided by the instrument and the locking solvent signal. Before integrating NMR peaks, the baseline in the regions of interest (i.e., 8–6 and ~ 3 ppm) was adjusted to zero. The ammonia concentrations were then obtained by integrating the $^{14}\text{NH}_4^+$ triplet peaks (8–6 ppm, with a spacing of 52.2 Hz)^{31,34} and the dimethyl sulfone singlet peak (~ 3 ppm).

DFT studies

Periodic plane-wave spin-polarized DFT calculations were performed to study the electronic structures and bulk energetics of metal nitrides. We used Perdew-Burke-Ernzerhof (PBE) functional⁷⁴ as implemented in the Vienna *ab initio* simulation package^{75,76} and projector augmented wave method⁷⁷ for the description of core-electron interaction, and the plane-wave cutoff was set to 550 eV. The used PBE functional was chosen to have a consistent method among the nitride chemistries studied, and the initial structure models were taken from the Materials Project database:⁷⁸ Fe_2N (mp-248), Ni_3N (mp-2033), WN (mp-569228), TiN (mp-492), NbN (mp-1580), VN (mp-925), ZrN (mp-1352), CrN (mp-2132), and Ta_3N_5 (mp-27488). DFT calculations for CrN were performed using an antiferromagnetic initial state in order to be consistent with previous experimental⁷⁹ and computational⁸⁰ observations for the magnetic ordering of CrN, while the DFT calculations for the other nitrides were performed using ferromagnetic initial states with resulting magnetic structures consistent with previous results, where only Fe_2N is ferromagnetic.⁸¹ The convergence threshold for electronic steps was 10^{-6} eV per unit cell, and the residual forces on all atoms were less than 10^{-2} eV \AA^{-1} . Metal d and nitrogen 2p band centers were determined by taking the centroid of the projected DOS of metal d and nitrogen 2p states relative to the Fermi level, respectively. The COHPs of these nitrides were computed using the LOBSTER program.⁸² More details are provided in the [supplemental information](#).

SUPPLEMENTAL INFORMATION

Supplemental information can be found online at <https://doi.org/10.1016/j.joule.2022.11.011>.

ACKNOWLEDGMENTS

The authors are grateful to Dr. Aaron Garg and Kaylee L. McCormack for the help in nitride synthesis, to Dr. Chaoyu Li for the help in Raman measurements, to Dr. Thanneer M. Narayanan for the help in SEM measurements, to Dr. Jonathan Hwang and Dr. Juan Corchado-García for the help in XES measurements, to Dr. Yijin Liu for the help in TXM XANES measurements, and to Dr. Kiarash Gordiz and Daniele Vivona for the discussion on DFT calculations. This work was funded by the Toyota Research Institute through the Accelerated Materials Design and Discovery program. J.J.G.-S. is grateful to the Generalitat Valenciana and the European Social Fund for their economic support in the form of Vali+d postdoctoral grant (APOSTD-2018-001). G.M.L. was partially supported by a Natural Sciences and Engineering Research Council of Canada (NSERC) PGS-D. This research used resources of the National Energy Research Scientific Computing Center (NERSC), a US Department of Energy Office of Science User Facility operated under contract no. DE-AC02-05CH11231. This work used the Extreme Science and Engineering Discovery Environment (XSEDE),⁸³ which is supported by the National Science Foundation grant number ACI-1548562. This work made use of the MRSEC Shared Experimental Facilities at MIT, supported by the National Science Foundation under award number DMR-1419807. This work was performed in part at the Center for Nanoscale Systems (CNS), a member of the National Nanotechnology Coordinated Infrastructure Network (NNCI), which is supported by the National Science Foundation under NSF award no. 1541959. CNS is part of Harvard University. Part of the research described in this paper was performed at the Canadian Light Source, a national research facility of the University of Saskatchewan, which is supported by the Canada Foundation for Innovation (CFI), the Natural Sciences and Engineering Research Council (NSERC), the National Research Council (NRC), the Canadian Institutes of Health Research (CIHR), the Government of Saskatchewan, and the University of Saskatchewan. Use of the Stanford Synchrotron Radiation Lightsource, SLAC National Accelerator Laboratory, is supported by the U.S. Department of Energy, Office of Science, Office of Basic Energy Sciences under contract no. DE-AC02-76SF00515.

AUTHOR CONTRIBUTIONS

Y.S.-H., Y.R.-L., and J.P. conceived the original idea. J.P. and Y.S.-H. designed the experiments. W.P.M. carried out the nitride synthesis. J.P. performed the characterization, dissolution experiments, and metal ion quantification. J.P., J.J.G.-S., and G.M.L. conducted the ammonia quantification. J.P. and L.G. carried out the DFT calculations. J.P. and Y.Y. participated in the synchrotron experiments. J.P. drafted the manuscript. All authors contributed to the revision of the manuscript.

DECLARATION OF INTERESTS

Y.S.-H. is a member of the Joule advisory board.

Received: May 2, 2022

Revised: October 26, 2022

Accepted: November 21, 2022

Published: December 19, 2022

REFERENCES

1. Wang, H., Li, J., Li, K., Lin, Y., Chen, J., Gao, L., Nicolosi, V., Xiao, X., and Lee, J.M. (2021). Transition metal nitrides for electrochemical energy applications. *Chem. Soc. Rev.* 50, 1354–1390.
2. Tian, D., Denny, S.R., Li, K., Wang, H., Kattel, S., and Chen, J.G. (2021). Density functional theory studies of transition metal carbides and nitrides as electrocatalysts. *Chem. Soc. Rev.* 50, 12338–12376.
3. Hu, B., Hu, M., Seefeldt, L., and Liu, T.L. (2019). Electrochemical dinitrogen reduction to ammonia by Mo₂N: catalysis or decomposition? *ACS Energy Lett.* 4, 1053–1054.

4. Du, H.L., Gengenbach, T.R., Hodgetts, R., Macfarlane, D.R., and Simonov, A.N. (2019). Critical assessment of the electrocatalytic activity of vanadium and niobium nitrides toward dinitrogen reduction to ammonia. *ACS Sustain. Chem. Eng.* 7, 6839–6850.
5. Manjunatha, R., Karajić, A., Teller, H., Nicoara, K., and Schechter, A. (2020). Electrochemical and chemical instability of vanadium nitride in the synthesis of ammonia directly from nitrogen. *ChemCatChem* 12, 438–443.
6. Stevens, M.B., Anand, M., Kreider, M.E., Price, E.K., Zeledón, J.Z., Wang, L., Peng, J., Li, H., Gregoire, J.M., Hummelshøj, J., et al. (2022). New challenges in oxygen reduction catalysis: a consortium retrospective to inform future research. *Energy Environ. Sci.* 15, 3775–3794.
7. Göhl, D., Garg, A., Paciok, P., Mayrhofer, K.J.J., Hegggen, M., Shao-Horn, Y., Dunin-Borkowski, R.E., Román-Leshkov, Y., and Ledendecker, M. (2020). Engineering stable electrocatalysts by synergistic stabilization between carbide cores and Pt shells. *Nat. Mater.* 19, 287–291.
8. Kreider, M.E., Gallo, A., Back, S., Liu, Y., Siahrostami, S., Nordlund, D., Sinclair, R., Nørskov, J.K., King, L.A., and Jaramillo, T.F. (2019). Precious metal-free nickel nitride catalyst for the oxygen reduction reaction. *ACS Appl. Mater. Interfaces* 11, 26863–26871.
9. Qiao, Z., Johnson, D., and Djire, A. (2021). Challenges and opportunities for nitrogen reduction to ammonia on transitional metal nitrides via Mars-van Krevelen mechanism. *Cell Rep. Phys. Sci.* 2, 100438.
10. Abghouli, Y., Garden, A.L., Howalt, J.G., Vegge, T., and Skúlason, E. (2016). Electroreduction of N₂ to ammonia at ambient conditions on mononitrides of Zr, Nb, Cr, and V: a DFT guide for experiments. *ACS Catal.* 6, 635–646.
11. Abghouli, Y., and Skúlason, E. (2017). Computational predictions of catalytic activity of zincblende (110) surfaces of metal nitrides for electrochemical ammonia synthesis. *J. Phys. Chem. C* 121, 6141–6151.
12. Matanović, I., Garzon, F.H., and Henson, N.J. (2014). Electro-reduction of nitrogen on molybdenum nitride: structure, energetics, and vibrational spectra from DFT. *Phys. Chem. Chem. Phys.* 16, 3014–3026.
13. McEnaney, J.M., Singh, A.R., Schwalbe, J.A., Kibsgaard, J., Lin, J.C., Cargnello, M., Jaramillo, T.F., and Nørskov, J.K. (2017). Ammonia synthesis from N₂ and H₂O using a lithium cycling electrification strategy at atmospheric pressure. *Energy Environ. Sci.* 10, 1621–1630.
14. Swearer, D.F., Knowles, N.R., Everitt, H.O., and Halas, N.J. (2019). Light-driven chemical looping for ammonia synthesis. *ACS Energy Lett.* 4, 1505–1512.
15. Michalsky, R., Avram, A.M., Peterson, B.A., Pfromm, P.H., and Peterson, A.A. (2015). Chemical looping of metal nitride catalysts: low-pressure ammonia synthesis for energy storage. *Chem. Sci.* 6, 3965–3974.
16. Tricker, A.W., Hebisch, K.L., Buchmann, M., Liu, Y.-H., Rose, M., Stavitski, E., Medford, A.J., Hatzell, M.C., and Sievers, C. (2020). Mechanocatalytic ammonia synthesis over TiN in transient microenvironments. *ACS Energy Lett.* 5, 3362–3367.
17. Han, G.-F., Li, F., Chen, Z.-W., Coppex, C., Kim, S.-J., Noh, H.-J., Fu, Z., Lu, Y., Singh, C.V., Siahrostami, S., et al. (2021). Mechanochemistry for ammonia synthesis under mild conditions. *Nat. Nanotechnol.* 16, 325–330.
18. Guo, J., and Chen, P. (2021). Interplay of alkali, transition metals, nitrogen, and hydrogen in ammonia synthesis and decomposition reactions. *Acc. Chem. Res.* 54, 2434–2444.
19. Fowler, G.J. (1901). XXIX.—iron nitride. *J. Chem. Soc. Trans.* 79, 285–299.
20. Ohkubo, I., and Mori, T. (2022). Rational design of 3d transition-metal compounds for thermoelectric properties by using periodic trends in electron-correlation modulation. *J. Am. Chem. Soc.* 144, 3590–3602.
21. Sun, W., Dacek, S.T., Ong, S.P., Hautier, G., Jain, A., Richards, W.D., Gamst, A.C., Persson, K.A., and Ceder, G. (2016). The thermodynamic scale of inorganic crystalline metastability. *Sci. Adv.* 2, e1600225.
22. Lee, Y.-L., Kleis, J., Rossmeisl, J., Shao-Horn, Y., and Morgan, D. (2011). Prediction of solid oxide fuel cell cathode activity with first-principles descriptors. *Energy Environ. Sci.* 4, 3966–3970.
23. Giordano, L., Østergaard, T.M., Muy, S., Yu, Y., Charles, N., Kim, S., Zhang, Y., Maglia, F., Jung, R., Lund, I., et al. (2019). Ligand-dependent energetics for dehydrogenation: implications in Li-ion battery electrolyte stability and selective oxidation catalysis of hydrogen-containing molecules. *Chem. Mater.* 31, 5464–5474.
24. Zhu, Y.G., Leverick, G., Giordano, L., Feng, S., Zhang, Y., Yu, Y., Tatara, R., Lunger, J.R., and Shao-Horn, Y. (2022). Nitrate-mediated four-electron oxygen reduction on metal oxides for lithium-oxygen batteries. *Joule* 6, 1887–1903.
25. Peng, J., Giordano, L., Davenport, T.C., and Shao-Horn, Y. (2022). Stability design principles of manganese-based oxides in acid. *Chem. Mater.* 34, 7774–7787.
26. Giordano, L., Akkiraju, K., Jacobs, R., Vivona, D., Morgan, D., and Shao-Horn, Y. (2022). Electronic structure-based descriptors for oxide properties and functions. *Acc. Chem. Res.* 55, 298–308.
27. Rao, R.R., Kolb, M.J., Giordano, L., Pedersen, A.F., Katayama, Y., Hwang, J., Mehta, A., You, H., Lunger, J.R., Zhou, H., et al. (2020). Operando identification of site-dependent water oxidation activity on ruthenium dioxide single-crystal surfaces. *Nat. Catal.* 3, 516–525.
28. Hwang, J., Rao, R.R., Giordano, L., Akkiraju, K., Wang, X.R., Crumlin, E.J., Bluhm, H., and Shao-Horn, Y. (2021). Regulating oxygen activity of perovskites to promote NO_x oxidation and reduction kinetics. *Nat. Catal.* 4, 663–673.
29. Garg, A., Milina, M., Ball, M., Zanchet, D., Hunt, S.T., Dumesic, J.A., et al. (2017). Transition-metal nitride core@noble-metal shell nanoparticles as highly CO tolerant catalysts. *Angew. Chem. Int. Ed.* 56, 8828–8833.
30. Katsura, M. (1992). Thermodynamics of nitride and hydride formation by the reaction of metals with flowing NH₃. *J. Alloys Compd.* 182, 91–102.
31. Iriawan, H., Andersen, S.Z., Zhang, X., Comer, B.M., Barrio, J., Chen, P., Medford, A.J., Stephens, I.E.L., Chorkendorff, I., and Shao-Horn, Y. (2021). Methods for nitrogen activation by reduction and oxidation. *Nat. Rev. Methods Primers* 1, 56.
32. Giner-Sanz, J.J., Leverick, G.M., Pérez-Herranz, V., and Shao-Horn, Y. (2020). Salicylate method for ammonia quantification in nitrogen electroreduction experiments: the correction of iron III interference. *J. Electrochem. Soc.* 167, 134519.
33. Giner-Sanz, J.J., Leverick, G., Pérez-Herranz, V., and Shao-Horn, Y. (2021). Optimization of the salicylate method for ammonia quantification from nitrogen electroreduction. *J. Electroanal. Chem.* 896, 115250.
34. Andersen, S.Z., Čolić, V., Yang, S., Schwalbe, J.A., Nielander, A.C., McEnaney, J.M., Enmark-Rasmussen, K., Baker, J.G., Singh, A.R., Rohr, B.A., et al. (2019). A rigorous electrochemical ammonia synthesis protocol with quantitative isotope measurements. *Nature* 570, 504–508.
35. Hong, W.T., Stoerzinger, K.A., Lee, Y.-L., Giordano, L., Grimaud, A.J.L., Johnson, A.M., Hwang, J., Crumlin, E.J., Yang, W., and Shao-Horn, Y. (2017). Charge-transfer-energy-dependent oxygen evolution reaction mechanisms for perovskite oxides. *Energy Environ. Sci.* 10, 2190–2200.
36. Hong, W.T., Stoerzinger, K.A., Moritz, B., Devereaux, T.P., Yang, W., and Shao-Horn, Y. (2015). Probing LaMO₃ metal and oxygen partial density of states using X-ray emission, absorption, and photoelectron spectroscopy. *J. Phys. Chem. C* 119, 2063–2072.
37. Peng, J., Schwalbe-Koda, D., Akkiraju, K., Xie, T., Giordano, L., Yu, Y., et al. (2022). Human- and machine-centred designs of molecules and materials for sustainability and decarbonization. *Nat. Rev. Mater.* 7, 991–1009.
38. Dronskowski, R., and Bloechl, P.E. (1993). Crystal orbital Hamilton populations (COHP): energy-resolved visualization of chemical bonding in solids based on density-functional calculations. *J. Phys. Chem.* 97, 8617–8624.
39. Rohling, R.Y., Tranca, I.C., Hensen, E.J.M., and Pidko, E.A. (2019). Correlations between density-based bond orders and orbital-based bond energies for chemical bonding analysis. *J. Phys. Chem. C* 123, 2843–2854.
40. Sun, W., Bartel, C.J., Arca, E., Bauers, S.R., Matthews, B., Orváñanos, B., Chen, B.R., Toney, M.F., Schelhas, L.T., Tumas, W., et al. (2019). A map of the inorganic ternary metal nitrides. *Nat. Mater.* 18, 732–739.
41. van Arkel, A.E. (1957). Molecules and crystals in inorganic chemistry. *J. Chem. Educ.* 34, 417.
42. Speck, F.D., Zagalskaya, A., Alexandrov, V., and Cherevko, S. (2021). Periodicity in the electrochemical dissolution of transition metals. *Angew. Chem. Int. Ed.* 60, 13343–13349.

43. Hwang, J., Rao, R.R., Giordano, L., Katayama, Y., Yu, Y., and Shao-Horn, Y. (2017). Perovskites in catalysis and electrocatalysis. *Science* 358, 751–756.
44. Kuznetsov, D.A., Peng, J., Giordano, L., Román-Leshkov, Y., and Shao-Horn, Y. (2020). Bismuth substituted strontium cobalt perovskites for catalyzing oxygen evolution. *J. Phys. Chem. C* 124, 6562–6570.
45. Glasson, D.R., and Jayaweera, S.A.A. (1968). Formation and reactivity of nitrides I. Review and introduction. *J. Appl. Chem.* 18, 65–77.
46. Göhl, D., Rueß, H., Pander, M., Zeradjanin, A.R., Mayrhofer, K.J.J., Schneider, J.M., Erbe, A., and Ledendecker, M. (2020). Transition metal–carbon bond enthalpies as descriptor for the electrochemical stability of transition metal carbides in electrocatalytic applications. *J. Electrochem. Soc.* 167, 21501.
47. Chen, M., Qi, J., Guo, D., Lei, H., Zhang, W., and Cao, R. (2017). Facile synthesis of sponge-like Ni₃N/NC for electrocatalytic water oxidation. *Chem. Commun.* 53, 9566–9569.
48. Huang, L., Yang, J., Zhou, W., Liu, K., Zhu, D., and Chen, Y. (2018). Nanoscale tungsten nitride/nitrogen-doped carbon as an efficient non-noble metal catalyst for hydrogen and oxygen recombination at room temperature in nickel–iron batteries. *RSC Adv.* 8, 35343–35347.
49. Zhu, Y., Chen, G., Zhong, Y., Zhou, W., and Shao, Z. (2018). Rationally designed hierarchically structured tungsten nitride and nitrogen-rich graphene-like carbon nanocomposite as efficient hydrogen evolution electrocatalyst. *Adv. Sci.* 5, 1700603.
50. Blesa, M.A., Morando, P.J., and Regazzoni, A.E. (1994). Chemical Dissolution of Metal Oxides (CRC Press).
51. Zinder, B., Furrer, G., and Stumm, W. (1986). The coordination chemistry of weathering: II. Dissolution of Fe(III) oxides. *Geochim. Cosmochim. Acta* 50, 1861–1869.
52. Laarz, E., Zhmud, B.V., and Bergström, L. (2000). Dissolution and deagglomeration of silicon nitride in aqueous medium. *J. Am. Ceram. Soc.* 83, 2394–2400.
53. Crundwell, F.K. (2014). The mechanism of dissolution of minerals in acidic and alkaline solutions: part I — a new theory of non-oxidation dissolution. *Hydrometallurgy* 149, 252–264.
54. Crundwell, F.K. (2016). The mechanism of dissolution of minerals in acidic and alkaline solutions: Part VI A molecular viewpoint. *Hydrometallurgy* 161, 34–44.
55. Hayes, K.F., and Katz, L.E. (1996). Application of X-ray absorption spectroscopy for surface complexation modeling of metal ion sorption. In *Physics and Chemistry of Mineral Surfaces* (CRC Press), pp. 147–233.
56. Sun, W., Kitchev, D.A., Kramer, D., and Ceder, G. (2019). Non-equilibrium crystallization pathways of manganese oxides in aqueous solution. *Nat. Commun.* 10, 573.
57. Chen, B.-R., Sun, W., Kitchev, D.A., Stone, K.H., Davis, R.C., Ceder, G., Schelhas, L.T., and Toney, M.F. (2021). Kinetic origins of the metastable zone width in the manganese oxide Pourbaix diagram. *J. Mater. Chem. A* 9, 7857–7867.
58. Allred, A.L. (1961). Electronegativity values from thermochemical data. *J. Inorg. Nucl. Chem.* 17, 215–221.
59. Kozejova, M., Latyshev, V., Kavcansky, V., You, H., Vorobiov, S., Kovalcikova, A., and Komaničky, V. (2019). Evaluation of hydrogen evolution reaction activity of molybdenum nitride thin films on their nitrogen content. *Electrochim. Acta* 315, 9–16.
60. Cao, B., Neuefeind, J.C., Adzic, R.R., and Khalifah, P.G. (2015). Molybdenum nitrides as oxygen reduction reaction catalysts: structural and electrochemical studies. *Inorg. Chem.* 54, 2128–2136.
61. Fritz, K.E., Yan, Y., and Suntivich, J. (2019). Influence of 3d transition-metal substitution on the oxygen reduction reaction electrocatalysis of ternary nitrides in acid. *Nano Res.* 12, 2307–2312.
62. Zhong, Y., Xia, X., Shi, F., Zhan, J., Tu, J., and Fan, H.J. (2016). Transition metal carbides and nitrides in energy storage and conversion. *Adv. Sci.* 3, 1500286.
63. Sun, W., Holder, A., Orváños, B., Arca, E., Zakutayev, A., Lany, S., and Ceder, G. (2017). Thermodynamic routes to novel metastable nitrogen-rich nitrides. *Chem. Mater.* 29, 6936–6946.
64. Jin, S. (2017). Are metal chalcogenides, nitrides, and phosphides oxygen evolution catalysts or bifunctional catalysts? *ACS Energy Lett.* 2, 1937–1938.
65. Abroshan, H., Bothra, P., Back, S., Kulkarni, A., Nørskov, J.K., and Siahrostami, S. (2018). Ultrathin cobalt oxide overlayer promotes catalytic activity of cobalt nitride for the oxygen reduction reaction. *J. Phys. Chem. C* 122, 4783–4791.
66. Kreider, M.E., Stevens, M.B., Liu, Y., Patel, A.M., Statt, M.J., Gibbons, B.M., Gallo, A., Ben-Naim, M., Mehta, A., Davis, R.C., et al. (2020). Nitride or oxynitride? Elucidating the composition–activity relationships in molybdenum nitride electrocatalysts for the oxygen reduction reaction. *Chem. Mater.* 32, 2946–2960.
67. Scott, S.B., Sørensen, J.E., Rao, R.R., Moon, C., Kibsgaard, J., Shao-Horn, Y., and Chorkendorff, I. (2022). The low overpotential regime of acidic water oxidation part II: trends in metal and oxygen stability numbers. *Energy Environ. Sci.* 15, 1988–2001.
68. Shen, T.-H., Spillane, L., Peng, J., Shao-Horn, Y., and Tileli, V. (2022). Switchable wetting of oxygen-evolving oxide catalysts. *Nat. Catal.* 5, 30–36.
69. MacFarlane, D.R., Cherepanov, P.V., Choi, J., Suryanto, B.H.R., Hodgetts, R.Y., Bakker, J.M., Ferrero Vallana, F.M., and Simonov, A.N. (2020). A roadmap to the ammonia economy. *Joule* 4, 1186–1205.
70. Yuan, S., Peng, J., Cai, B., Huang, Z., García-Esparza, A.T., Sokaras, D., Zhang, Y., Giordano, L., Akkiraju, K., Zhu, Y.G., et al. (2022). Tunable metal hydroxide–organic frameworks for catalysing oxygen evolution. *Nat. Mater.* 21, 673–680.
71. Peng, J., Damewood, J.K., Karaguesian, J., Gómez-Bombarelli, R., and Shao-Horn, Y. (2021). Navigating multimetallic catalyst space with Bayesian optimization. *Joule* 5, 3069–3071.
72. Bower, C.E., and Holm-Hansen, T. (1980). A salicylate–hypochlorite method for determining ammonia in seawater. *Can. J. Fish. Aquat. Sci.* 37, 794–798.
73. Le, P.T.T., and Boyd, C.E. (2012). Comparison of phenate and salicylate methods for determination of total ammonia nitrogen in freshwater and saline water. *J. World Aquac. Soc.* 43, 885–889.
74. Perdew, J.P., Burke, K., and Ernzerhof, M. (1996). Generalized gradient approximation made simple. *Phys. Rev. Lett.* 77, 3865–3868.
75. Kresse, G., and Hafner, J. (1993). Ab initio molecular dynamics for liquid metals. *Phys. Rev. B Condens. Matter* 47, 558–561.
76. Kresse, G., and Furthmüller, J. (1996). Efficient iterative schemes for ab initio total-energy calculations using a plane-wave basis set. *Phys. Rev. B Condens. Matter* 54, 11169–11186.
77. Blöchl, P.E. (1994). Projector augmented-wave method. *Phys. Rev. B Condens. Matter* 50, 17953–17979.
78. Jain, A., Ong, S.P., Hautier, G., Chen, W., Richards, W.D., Dacek, S., Cholia, S., Gunter, D., Skinner, D., Ceder, G., et al. (2013). Commentary: the Materials Project: a materials genome approach to accelerating materials innovation. *APL Mater.* 1, 11002.
79. Corliss, L.M., Elliott, N., and Hastings, J.M. (1960). Antiferromagnetic structure of CrN. *Phys. Rev.* 117, 929–935.
80. Filippetti, A., Pickett, W.E., and Klein, B.M. (1999). Competition between magnetic and structural transitions in CrN. *Phys. Rev. B* 59, 7043–7050.
81. Bainbridge, J., Channing, D.A., Whitlow, W.H., and Pendlebury, R.E. (1973). A Mössbauer and X-ray investigation of ξ -Fe₂N. *J. Phys. Chem. Solids* 34, 1579–1586.
82. Maintz, S., Deringer, V.L., Tchougréeff, A.L., and Dronskowski, R. (2016). LOBSTER: a tool to extract chemical bonding from plane-wave based DFT. *J. Comput. Chem.* 37, 1030–1035.
83. Towns, J., Cockerill, T., Dahan, M., Foster, I., Gaither, K., Grimshaw, A., Hazlewood, V., Lathrop, S., Lifka, D., Peterson, G.D., et al. (2014). XSEDE: accelerating scientific discovery. *Comput. Sci. Eng.* 16, 62–74.